

A Carrier-free Peptide Co-assembled System with Synergistic Antitumor Effect Combines Immunotherapy and Sonodynamic Therapy

Limin Zhang¹, Weizhi Wang^{1*}

1. Key Laboratory of Medical Molecule Science and Pharmaceutics Engineering, Ministry of Industry and Information Technology, Key Laboratory of Cluster Science of Ministry of Education, Beijing Key Laboratory of Photoelectronic/Electro-photon Conversion Materials, School of Medical Technology, School of Chemistry and Chemical Engineering, Beijing Institute of Technology, Beijing 100081, P. R. China.

Abstract

Blocking programmed cell death ligand 1 (PD-L1) in tumor cells is an effective therapy strategy to achieve immune system activation for tumor therapy, however only a few patients can benefit from it. Development of synergistic therapy with checkpoint PD-L1 blockade immunotherapy is beneficial to enhance antitumor effect. Herein, we constructed a carrier-free system EH@Ag₂S co-assembled by peptide nanofiber and Ag₂S nanoparticles to achieve a superadditive (1 + 1 > 2) antitumor effect. EH nanofiber can block PD-L1, and Ag₂S can produce reactive oxygen species (ROS) under ultrasound irradiation and induce cell apoptosis. Further, *in vivo* mice experiment also confirmed the high efficiency of this carrier-free co-assembled system in successfully inducing anti-tumor response while inhibiting tumor growth. We believe that this highly bioavailable and multifunctional therapeutic system may become a promising nanoplatform for tumor therapy.

KEYWORDS: *peptide, Immune checkpoint blockade, sonodynamic therapy, co-assembly*

1. Introduction

Traditional treatment methods, including chemotherapy and radiotherapy, have limited therapeutic effects, and the side effects may cause unexpected damage to patient's normal tissues, which may accelerate the deterioration of the patient's condition or even threaten life[1]. Therefore, new therapeutic methods need to be developed to improve the tumor therapeutic effects. Immune checkpoint blockade (ICB) immunotherapy has achieved remarkable tumor inhibitory effects by activating endogenous anti-tumor T cells to kill cancer cells. Among multiple checkpoint inhibitors, programmed death 1 (PD-1) and its predominant ligand, programmed death ligand 1 (PD-L1) are key immune checkpoint molecules, which are closely related to immune resistance[2]. Blocking the PD-1/PD-L1 pathway is expected to rejuvenate exhausted CD8⁺ T cells to boost anti-tumor immune responses[3, 4]. Currently, most checkpoint inhibitors targeting the PD-1/PD-L1 are monoclonal antibodies[5]. Although antibodies have demonstrated a durable tumor regression, the large size of antibodies causes poor deep penetration for solid tumor, and the excessive half-life may cause immune-related adverse events.

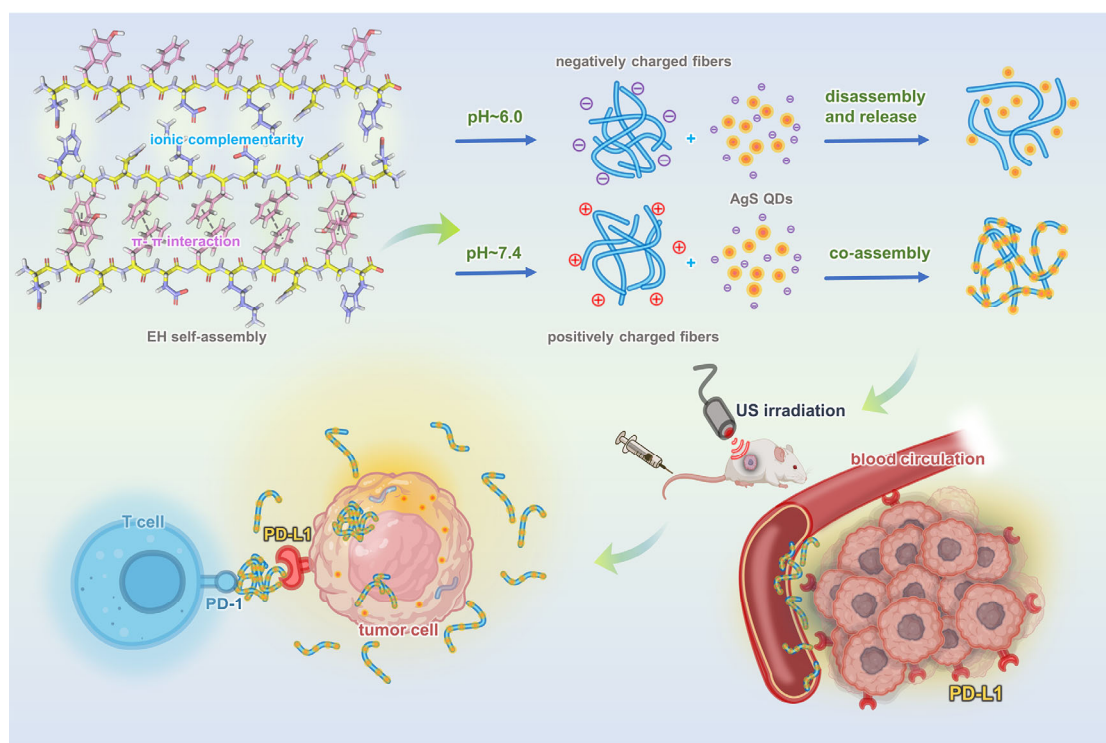
Targeting peptides have a standard synthetic protocol, can be artificially designed and modified with satisfactory biocompatibility[6, 7]. They have become potent inhibitors of ICB. Through rational design, peptide-based PD-L1 inhibitors can form supramolecular assemblies, which enhance their stability in blood circulation and resistance to enzymatic hydrolysis[8]. Moreover, their activities can be further improved by self-assembly due to the increased local density of the peptide[9]. In addition, based on the 'customizable assembly' of peptides, researchers have also combined self-assembling peptides with nanomaterials to develop multifunctional antitumor systems. Most of these systems connect peptides and nanomaterials through covalent bonds[10, 11]. However, the covalent synthesis reaction steps are cumbersome, and may involve a large number of separation and purification processes. Moreover, coupling peptides to liposome[12] or polymer micelles[13, 14], etc., have been explored as co-delivery carriers to physically package nanomaterials. In terms of structures and

functions of these additional introduced carrier are relatively fixed, they are not dynamic enough to respond flexibly to various stimuli. Due to flexible control and easy operation of non-covalent interactions, peptide also can bind to nanomaterials through non-covalent interactions to construct multifunctional structures. And those strategies are mainly including hydrogen bonding[15, 16], electrostatic interaction[17, 18], hydrophobic interaction[19-21] and π - π interaction[22, 23]. Based on the above, we assume that peptide-based PD-L1 inhibitors interact with therapeutic nanomaterials through non-covalent interactions, an intelligent carrier-free antitumor system may be engineered to enhance tumor therapy effect and reduce the potential toxicity of nanomaterials.

Although ICB has significant tumor suppressor efficacy in the tumor treatments, only a few patients benefit from it[24-26]. A critical reason for this phenomenon is that the insufficient infiltration of T cells into tumors causing poor immune response[25-28]. In recent years, novel approaches to boost the antitumor immune response, such as photothermal therapy (PPT), photodynamic therapy (PDT), sonodynamic therapy (SDT) and etc., have recently gained increased interest. SDT, as a non-invasive therapy, hold the advantages of strong tissue penetration and little damage to normal tissues. Sonodynamic therapy can induce highly toxic reactive oxygen species (ROS) in tumor to kill tumor cells in the presence of sonosensitizers and low-intensity ultrasound-induced sonosensitizers[29-31]. SDT complements the lack of patient response to immunotherapy by increasing the infiltration of CD8⁺ T cells[32, 33]. Clinical animal experiments have shown that tumor cell fragments produced by SDT can be considered as tumor antigens to trigger host anti-tumor immune response[34]. Therefore, we envision that integrating ICB immunotherapy and SDT may provide an advanced nanoplatform for effective tumor treatment. Combination of checkpoint inhibition through anti-PD-L1 antibody and SDT was also recently reported for treatment of metastatic breast tumor and showed exciting effect[35].

Herein, we describe a carrier-free co-assembled system of dual therapeutic agents that combines immunotherapy and sonodynamic therapy to enhance antitumor therapy

(Scheme 1). Firstly, we obtained an ion complementary peptide compound EH (sequence: EYNFDFKFNYH) that can target PD-L1 through the peptide library construction and screening strategy previously developed in our group[36-38]. Secondly, the EH can self-assemble into nanofibers, the charged residues D, E, K and H in EH can stack into β -sheets through electrostatic interactions and endue the EH ‘pH-responsive switch’[39].The introduction of nonpolar residues Y and F further can stabilize the supramolecular structure through hydrophobic interactions[38]. Thirdly, the EH can co-assembly with the negatively charged Ag₂S via electrostatic interactions (EH@Ag₂S) at pH>6.0. The formation of the EH@Ag₂S co-assembly plays a better role in encapsulating Ag₂S, solving Ag₂S inability to target and specifically recognize tumor cells. In addition, due to Ag₂S small size, they usually identified as a foreign body by the reticuloendothelial system[40]. The co-assembled system we constructed effectively avoids itself easy to be metabolic excreted during blood circulation and insufficient tumor accumulation[41, 42]. For *in vivo*, EH can programmatically recognize and block PD-L1, after entering the cell then release Ag₂S owing to pH transformation changes the EH surface charge makes the electrostatic interaction between EH and Ag₂S disappear. Ag₂S can induce cell apoptosis through generating highly toxic ROS under the activation of US irradiation, which synergistically promotes the tumor immune microenvironment improvement. Overall, co-assembled system EH@Ag₂S may serve as potential candidates for antibody-free immune checkpoint inhibition, and SDT provides an alternative strategy for amplifying ICB immunotherapy to achieve a remarkable superadditive (1 + 1 > 2) antitumor effect.



Scheme 1. Schematic illustration of the carrier-free co-assembled system for PD-L1 blockade and sonodynamic therapy.

2. Materials and methods

2.1 Peptide EH synthesis and EH@Ag₂S synthesis

The sequence of the peptide was expressed as EYNFDFKFNYH. The peptides were synthesized by the general solid-phase peptide synthesis (Fmoc-SPPS) methodology on Wang resin. Then, the peptide EH was obtained and purified by high performance liquid chromatography (HPLC). Next, 50 μL of Ag₂S solution (2 mg mL⁻¹) was mixed with 950 μL of EH solution (2 mg mL⁻¹) and uniformly dispersed by ultrasonic. Then, the pH value of the above mixed solution was adjusted to 7.4 with 1 mM NaOH solution. After aging for 72 h, excess EH was removed by dialysis using the dialysis bag with a molecular weight cut-off of 1,600. EH@Ag₂S solution was obtained.

2.2 Cell-level validation of peptide targeting

The mouse colorectal cancer cells MC38 and the human embryonic kidney cells HEK-293T were seeded in 35-mm confocal dishes at a concentration of 1×10^5 mL⁻¹ and cultured overnight for cell adherence. FITC-labeled EH (FITC-EH) was dissolved in cold PBS at a concentration of 0.5 mg mL⁻¹. The cells were then washed three times

with cold PBS and incubated with Hoechst 33342 ($10 \mu\text{g mL}^{-1}$, $200 \mu\text{L}$) at $4 \text{ }^\circ\text{C}$ for 15 min. Then, the cells were washed three times with cold PBS, and incubated with the prepared FITC-EH solution (0.5 mg mL^{-1} , $200 \mu\text{L}$) at $4 \text{ }^\circ\text{C}$ for 15 min. Finally, the cells were washed three times with cold PBS. All the above operations were performed in the dark. Confocal fluorescence imaging was performed on confocal laser scanning microscope (CLSM).

2.3 Reactive oxygen species generation.

1,3-Diphenylisobenzofuran (DPBF) was employed as a chemical probe to evaluate the ROS generation production. 10 mg DPBF was dissolved in 1 mL DMSO to form a stable solution (37 mmol L^{-1}). An amount of EH@Ag₂S ($50 \mu\text{g mL}^{-1}$) was dispersed evenly in a quartz cell, and then $50 \mu\text{L}$ DPBF-DMSO solution was added. After continuous US irradiation (1.0 W cm^{-2} , 1.0 MHz , 50% duty free), the absorbance changes of DPBF at 424 nm were recorded to quantify the ROS generation rate.

2.4 *In vitro* ROS generation on cellular level.

MC38 cells were seeded in 6-well plates at a concentration of $1 \times 10^5 \text{ mL}^{-1}$ and cultured overnight for cell adherence. Eight groups (1) PBS +US, (2) EH +US, (3) Ag₂S +US, (4) EH@Ag₂S +US, (5) PBS -US, (6) EH -US, (7) Ag₂S -US, and (8) EH@Ag₂S -US were set to explore the potential of EH@Ag₂S in producing ROS upon exposure to US irradiation. In brief, MC38 cells were incubated with EH@Ag₂S ($50 \mu\text{g mL}^{-1}$) at $37 \text{ }^\circ\text{C}$ for 4 h. After incubation, the cells were irradiated with/without US irradiation (1.0 W cm^{-2} , 1.0 MHz , 50% duty free, 5 min). Immediately, DCFH-DA was added to each plate for 30 min in the dark. Finally, the cells were washed with PBS three times and then observed by CLSM.

2.5 Live/Dead staining

MC38 cells were seeded into 35-mm confocal dishes at a concentration of $1 \times 10^5 \text{ mL}^{-1}$ and cultured overnight for cell adherence. To verify the treatment effect on cell level, the cells were divided into eight groups and cultured with PBS, EH, Ag₂S, and EH@Ag₂S for 8 h, respectively: (1) PBS + US, (2) EH + US, (3) Ag₂S + US, (4) EH@Ag₂S + US, (5) PBS - US, (6) EH - US, (7) Ag₂S - US, and (8) EH@Ag₂S - US.

After the cells were treated as mentioned above (with or without US Irradiation) and then incubated for another 16 h. Then the cells were successively stained with 200 μL annexin Calcein-AM (2 μM) and PI (4.5 μM) for 20 min. Finally, the cells were washed three times with cold 1 \times Assay Buffer. All the above operations were performed in the dark. Confocal fluorescence imaging was performed to observe the live and dead cells distribution through the fluorescence distribution of Calcein-AM and PI.

2.6 *In vivo* therapy assay in mice model

Female C57BL/6N mice (6-8-week-old) with weighing approximately 18-20 g were selected. The MC38 tumor models were successfully established by subcutaneous injection of 4×10^6 cells suspended in 100 μL of PBS into the right lower limb below the skin of each mouse. After the tumors developed to approximately 50 mm^3 , *in vivo* tumor suppression studies were carried out. The tumor-bearing mice were randomly divided into six groups (n = 6, each group), and treated with (1) PBS, (2) US irradiation, (3) Ag₂S under US laser irradiation, (4) PD-L1 antibody, (5) EH and (6) EH@Ag₂S under US laser irradiation, respectively. All animal studies were conducted in accordance with the guidelines of the National Regulation of China for Care and Use of Laboratory Animals. Nanomaterials were injected through the tail vein, and each injection was 200 μL . For group (2), (3) and (6), the tumors were exposed to US irradiation (1.0 W cm^{-2} , 1.0 MHz, 50% duty free) for 3 min after the injection for 6 h and 9 h. Mice were treated three times and observed for 10 days after treatment. The body weight and tumor volume of each mouse were monitored every two days, and after 14 days treatment, the tumors were dissected and weighed to evaluate the therapeutic efficacy. All mice were kept and treated according to protocols approved by the Institutional Animal Care and Use Committee at the Ethics Committee of Animal Experiment Center, Beijing Institute of Technology. Approval number: 2016-0006-M-2020013.

2.7 Histopathological and immunohistochemical staining analysis of treatment effects

After treatment, the main internal organs and tumor tissues were removed for

hematoxylin and eosin (H&E) staining to observe cell morphology, Terminal dUTP Nick End Labeling (TUNEL) staining to evaluate cell apoptosis and collagen deposition, CD8⁺ T staining to determine whether inhibiting immunosuppressive cells leads to enhanced T cell response and interleukin-2 (IL-2) staining to check the activities of the tumor-associated immune microenvironment, interferon- γ (IFN- γ) staining to verify anti-tumor and immunoregulatory effects, calreticulin (CRT) staining to evaluate the degree of immunogenic death of tumor cells.

2.8 Statistical analysis

All data were reported as the mean \pm standard deviation (SD) unless otherwise stated. The level of statistical significance (*, $P \leq 0.05$, **, $P \leq 0.01$, ***, $P \leq 0.001$, $n = 6$) was defined by one-way analysis of variance (ANOVA) using OriginPro (Ver. 9.0). All graphs were drawn by Origin 2021.

3. Results and discussion

3.1 Design, preparation, and affinity validation of EH

To obtain a carrier-free co-assembled system, the “one-bead-one-compound (OBOC)” combinatorial chemistry approach was used to construct a PD-L1-targeting peptide library with a diversity of 10^6 . The OBOC peptide library with a NH₂-EX₁₀X₉X₈X₇X₆X₅X₄X₃X₂X₁-COOH motif was designed and synthesized. In this library, the X₁X₃X₅X₇X₉ position were diversified with hydrophilic and electric residues including T, D, K, H, E, S, N and Q. The X₂X₄X₆X₈X₁₀ position were diversified with hydrophobic residues including F, Y, W, I, V, A and Y. Through our previous screening protocols[36, 37], a PD-L1 targeting ion-complementary peptide EH (sequence: EYNFDFKFNYH) was selected. The molecular structure of EH was shown in **Fig. 1A**. EH was synthesized by Fmoc solid-phase synthesis, and the chemical structure and purity of EH was confirmed by MALDI-TOF-MS and high performance liquid chromatography (HPLC) (**Fig. S1**, **Fig. S2**). Furthermore, the binding behavior was monitored through surface plasmon resonance imaging (SPRi) to understand the

interaction of EH and PD-L1 protein. The dissociation constants K_D of EH was calculated as 7.79×10^{-7} M (**Fig. 1B**), indicating satisfactory affinity toward PD-L1. And the value also demonstrated higher binding ability than the intrinsic receptor PD-L1[43]. Next, molecular docking simulations were performed between EH and PD-L1 protein to predict the detail binding sites. As shown in **Fig. 1C**, the intermolecular forces between EH and PD-L1 protein were dominated by π - π interaction and hydrogen bonds. The docking region was located in the hot spot of PD-L1[44]. EH formed hydrogen bond interactions with residues Arg125 and π - π interaction with residues Tyr123 of PD-L1. Cellular level experiments further verified the specificity of EH towards PD-L1. The PD-L1 over-expressed mouse colorectal cancer cell line MC38 was served as a PD-L1⁺ cell model. The human embryonic kidney cell line HEK-293T with low PD-L1 expression was selected as a PD-L1⁻ cell model. Fluorescein isothiocyanate (FITC)-labeled EH (FITC-EH) was synthesized and the molecular weight of FITC-EH was confirmed by MALDI-TOF-MS (**Fig. S3**). Confocal laser scanning microscope (CLSM) results showed that FITC-EH could bind to PD-L1⁺ cells specifically with a high affinity, showing a bright fluorescent signal (**Fig. 1D and Fig. 1E**). The specificity of EH was also evaluated on gene silencing cell models. As shown in **Fig. 1F**, for PD-L1-siRNA-transfected MC38, the FITC-EH binding signal was decreased compared with untreated cells. All these above results indicated that EH could target PD-L1 with high affinity and specificity.

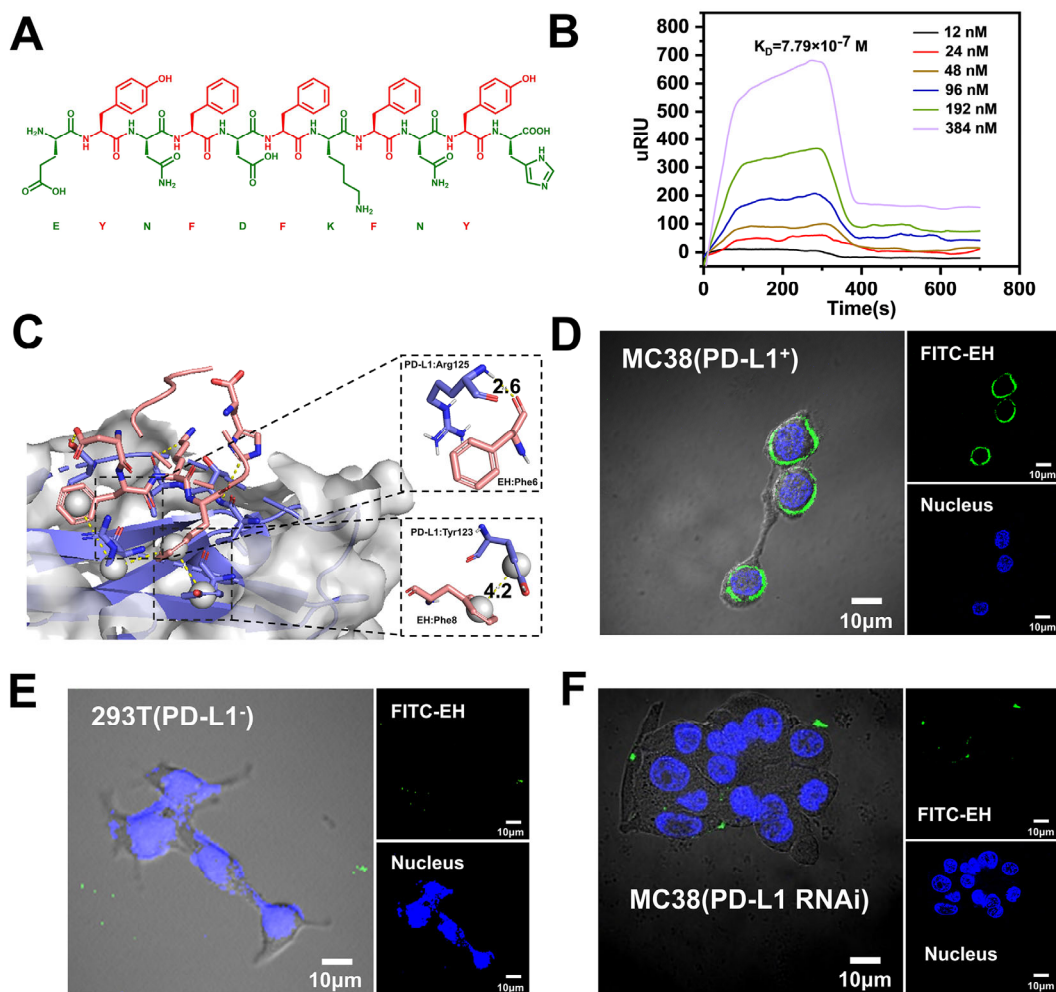


Fig.1 Specificity confirmation of the EH toward PD-L1. **(A)** Molecular formula of EH. **(B)** Binding affinity of EH toward PD-L1 by surface plasmon resonance imaging (SPR) detection. **(C)** Molecular docking for EH toward PD-L1. And the main binding sites between EH and PD-L1. **(D)** Confocal images of targeting ability of FITC-EH to MC38 cells. **(E)** Confocal images of targeting ability of FITC-EH to HEK-293T cells. **(F)** Confocal images of PD-L1-siRNA-transfected MC38 cells incubated with FITC-EH.

3.2 Preparation and characterization of EH and EH@Ag₂S

Different from the ‘building block’ (recognition unit, signal unit, self-assembly unit, etc.) construction mode of most existing peptide systems[45, 46]. When constructing the peptide library, the synergistic effect of peptide structure and function was fully considered. Alternating charge (or polarity) and hydrophobic amino acids were used to construct peptide library to obtain the peptides with the property of target recognition and self-assembly. Therefore, in the following experiments, the self-assembly performance of EH was verified. Atomic force microscope (AFM) and Transmission

electron microscope (TEM) micrographs of **Fig. 2D**, **Fig. 2G** showed the morphology of self-assembled EH. The EH could self-assemble into nanofibers with average diameters of 6.6 nm. The secondary structure formed by EH self-assembly was verified by circular dichroism (CD). As shown in **Fig. 2J**, the CD spectrum of EH had a positive peak at around 195 nm and a negative peak at around 215 nm, indicating the formation of a β -sheet structure.

Since EH system contained labile protons, we envisioned that regulating the pH of the system may alter the charge state of the EH, which may further affect the interaction with the Ag₂S[47]. Firstly, the zeta potential of EH and Ag₂S at different pH were measured. As shown in **Fig. 2A** and **Fig. 2B**, it was found that the EH supramolecular assembly were positively charged in normal physiological conditions (pH 7.4), and the Ag₂S were negatively charged whether in normal physiological conditions (pH 7.4) or tumor slightly acidic conditions (pH 6.0). Therefore, we envisaged that EH and Ag₂S could co-assemble to form supramolecular structures through electrostatic adsorption interaction at pH 7.4. By adjusting the mass ratio of EH and Ag₂S (**Fig. S4**), we tried to make Ag₂S adsorb on the EH fiber surface without affecting the formation process of EH fibers. Through our experiments, when EH was mixed with the Ag₂S at mass ratios of 4:1, Ag₂S and EH scattered on the surface of mica slices. We speculated that the high content of Ag₂S affected the longitudinal growth of EH fibers. When the mass ratio was adjusted to 5:1, EH nanofiber could be observed to start growing. When the mass ratio was adjusted to 10:1, stable short fibers of EH could be observed. However, the distribution of Ag₂S on EH was not enough. When the mass ratio was 20:1, Ag₂S could be uniformly distributed on the nanofibers to construct EH@Ag₂S co-assembly. The morphology of EH@Ag₂S was observed by AFM and TEM. It was found in **Fig. 2E** and **Fig. 2H** that Ag₂S could be uniformly distributed on the nanofibers. The sizes of the EH@Ag₂S were measured by dynamic light scattering (DLS). DLS showed two peaks, i.e., 30 and 3100 nm, which indicated the diameter and the length of the EH@Ag₂S (**Fig. S5**). The formation of co-assembled system EH@Ag₂S was also confirmed by energy dispersive spectroscopy (EDS) mapping with the distribution of

C, N, O, Ag and S. Through experiments, it was found that large amounts of Ag₂S were dispersed on the surface of nanofibers. C, N, O, Ag, and S exhibited the high uniformity of each element distribution (**Fig. 2L**). In addition, to verify whether the co-assembly affects the affinity of EH for PD-L1, we determined the binding affinity of the EH@Ag₂S co-assemblies using SPRi. The results showed that the K_D of EH@Ag₂S for PD-L1 was 6.67×10^{-7} M (**Fig. 2K**), similar to the affinity of EH for PD-L1 (K_D= 7.79×10^{-7} M). In subsequent experiments, we adjusted the pH of the system to less than 6.0 and found that decreased pH led to charge reversal of EH supramolecular assembly. As shown in **Fig. 2C**, the surface charge of EH supramolecular assembly and Ag₂S was negatively charged, leading to the electrostatic attraction between the Ag₂S and EH disappeared. This result was also confirmed by AFM and TEM image in **Fig. 2F** and **Fig. 2I**, co-assembled system EH@Ag₂S could not be observed when the pH changed to less than 6.0. EH and the Ag₂S were randomly scattered on the substrate. We speculated that Ag₂S could be released from the co-assembled system EH@Ag₂S as the pH decreased less than 6.0. Overall, it could be concluded that electrostatic attraction was the main factor driving the formation of EH@Ag₂S.

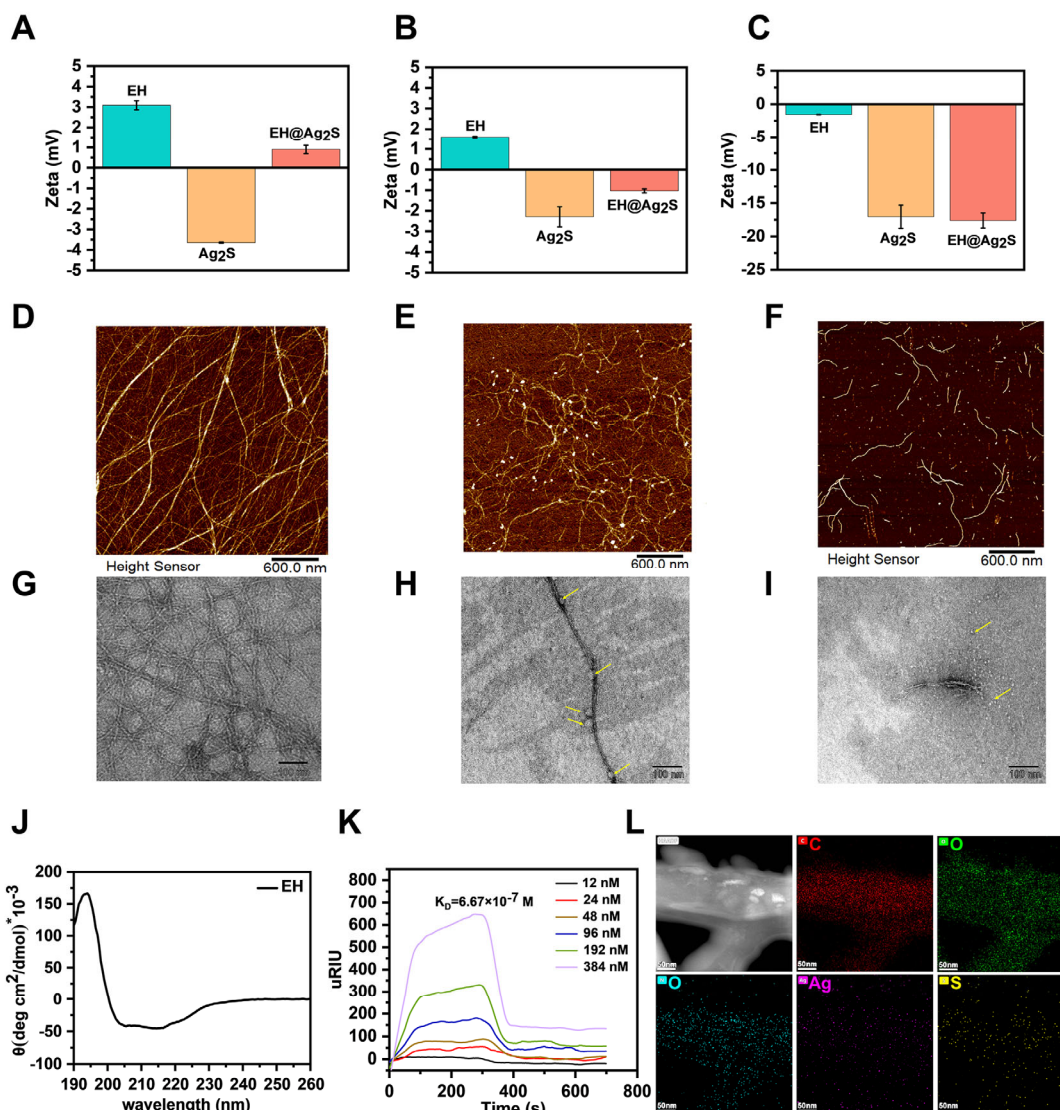


Fig. 2 Characterization of EH and EH @Ag₂S co-assembled structures. **(A)**, **(B)** and **(C)** The zeta potential of the EH, Ag₂S and EH@Ag₂S at pH 7.4, 6.0 and <math><6.0</math>. **(D)** Atomic force microscope (AFM) image of EH assembly morphology. **(E)** AFM image of EH@Ag₂S co-assembly morphology (pH 7.4). **(F)** AFM image of EH and Ag₂S (pH<6.0). **(G)** Transmission electron microscopy (TEM) image of EH assembly morphology. **(H)** TEM image of EH@Ag₂S co-assembly morphology (pH 7.4). The yellow arrows indicated Ag₂S. **(I)** TEM image of EH and Ag₂S (pH<6.0). The yellow arrows indicated Ag₂S. **(J)** Circular dichroism (CD) spectra of EH. **(K)** Binding affinity of EH@Ag₂S toward PD-L1 by SPRi detection. **(L)** Element mappings of EH@Ag₂S. Data were shown as mean \pm SD (n = 3).

3.3 SDT efficacy of EH@Ag₂S against cancer cells *in vitro*

Based on the fact that US irradiation can promote Ag₂S to generate ROS (**Fig. S6**)[48], the sonodynamic performance of the EH@Ag₂S was further evaluated. To

evaluate the ROS generation ability of EH@Ag₂S under US irradiation, 1,3-diphenylisobenzofuran (DPBF) was utilized to indicate the ability of ROS production outside the cell. As shown in **Fig. 3A**, under prolonged US irradiation (1.0 W cm⁻², 1.0 MHz, 50% duty free), the characteristic absorption peak of DPBF decreased significantly. Moreover, the variation of DPBF absorbance peak value at 424 nm relative to the initial value were recorded for different US irradiation time. As shown in **Fig. 3B** and **Fig. S6**, the DPBF concentration of Ag₂S group and EH@Ag₂S group decreased with 60.9% and 53.9% after 6min, respectively. However, after prolonged US irradiation, the characteristic peak of H₂O group decreased was not obvious (**Fig. S7**). EH@Ag₂S almost had no effect on the ROS generation ability of Ag₂S, and follow-up experiments could be carried out.

Further, the antitumor effect of EH@Ag₂S was evaluated *in vitro*. EH@Ag₂S cytotoxicity was investigated by standard cell counting kit-8 (CCK-8) assay. The toxicity of nano-system was first investigated, for MC38 cells and HEK-293T cells, EH@Ag₂S had no obvious toxicity in the absence of US irradiation for a further 24 h incubation (**Fig. 3C**). In the presence of US irradiation with a power density of 1.0 W cm⁻², the increase of EH@Ag₂S concentration produced more significant toxicity to MC38 cells. When the concentration of EH@Ag₂S was 50 μg mL⁻¹, nearly 83% of the MC38 cells were dead (**Fig. 3D**). Further, eight controls were established: (1) PBS +US, (2) EH +US, (3) Ag₂S +US, (4) EH@Ag₂S +US, (5) PBS -US, (6) EH -US, (7) Ag₂S -US, and (8) EH@Ag₂S -US to validate the degree of ROS production at the cellular level. 2,7-dichloro-dihydro-fluorescein diacetate (DCFH-DA) probe was used to detect intracellular ROS production. As shown in **Fig. 3E**, in the absence of US irradiation, no fluorescence was observed in any group. In the presence of US irradiation with a power density of 1.0 W cm⁻², the green fluorescence appeared in Ag₂S and EH@Ag₂S group, suggesting that different levels of ROS production were seen in these groups. The fluorescence intensity of the EH@Ag₂S group was higher than Ag₂S group, indicating the strongest ROS production level. While, in the PBS and EH group, no obvious fluorescence was observed, indicating that the US stimulation had no effect on

the ROS production by cells. Furthermore, the cell-killing effect on MC38 cells was verified after different treatments: (1) PBS +US, (2) EH +US, (3) Ag₂S +US, (4) EH@Ag₂S +US, (5) PBS -US, (6) EH -US, (7) Ag₂S -US, and (8) EH@Ag₂S -US by live/dead staining (calcein AM/PI) experiments. It had been found that the introduction of EH@Ag₂S combined with US stimulation (1.0 W cm⁻², 1.0 MHz, 50% duty free) significantly induced MC38 cells death, and treatment effect was consistent with the ROS production (**Fig. 3F**). These results indicated that EH@Ag₂S co-assembly could generate a large number of ROS, and the ROS generation could be further enhanced compared with Ag₂S at the cellular level, which might be relevant to the targeting effect of EH that enhanced the cell uptake of EH@Ag₂S.

Furthermore, to test whether co-assembly affect the PD-L1 blocking ability of EH at the cellular level, a competition experiment between EH monomer, EH assembly, EH@Ag₂S and the natural ligand PD-1 was performed to verify the checkpoint blocking ability. As shown in **Fig. 3G**, when PD-1 was incubated with MC38 cells, a large amount of PD-1 was distributed on the cell membrane. However, when PD-1 was co-incubated with EH monomer, EH assembly, and EH@Ag₂S with cells, respectively, the localization of PD-1 on cell membrane was disturbed, suggesting that different forms of EH did not affect the PD-L1 blocking ability of EH itself. In addition, to study the tumor inhibition effect, tumor cells were co-incubated with T cells after incubation with the EH, antibody and EH@Ag₂S, respectively (**Fig. 3I**). As shown in **Fig. 3H**, a growing number of T cells surrounded the cancer cells with increasing incubation time. And the cancer cells viability was investigated by CCK-8 assay. As shown in **Fig. 3J**, the viability of the EH@Ag₂S-treated group was evidently decrease compared with the PBS-treated group even stronger than the antibody-treated group. The results indicated that EH@Ag₂S restored the T cell antitumor response. In general, all the results demonstrated that EH@Ag₂S could provide robust tumor inhibition and achieve tumor therapy synergistically.

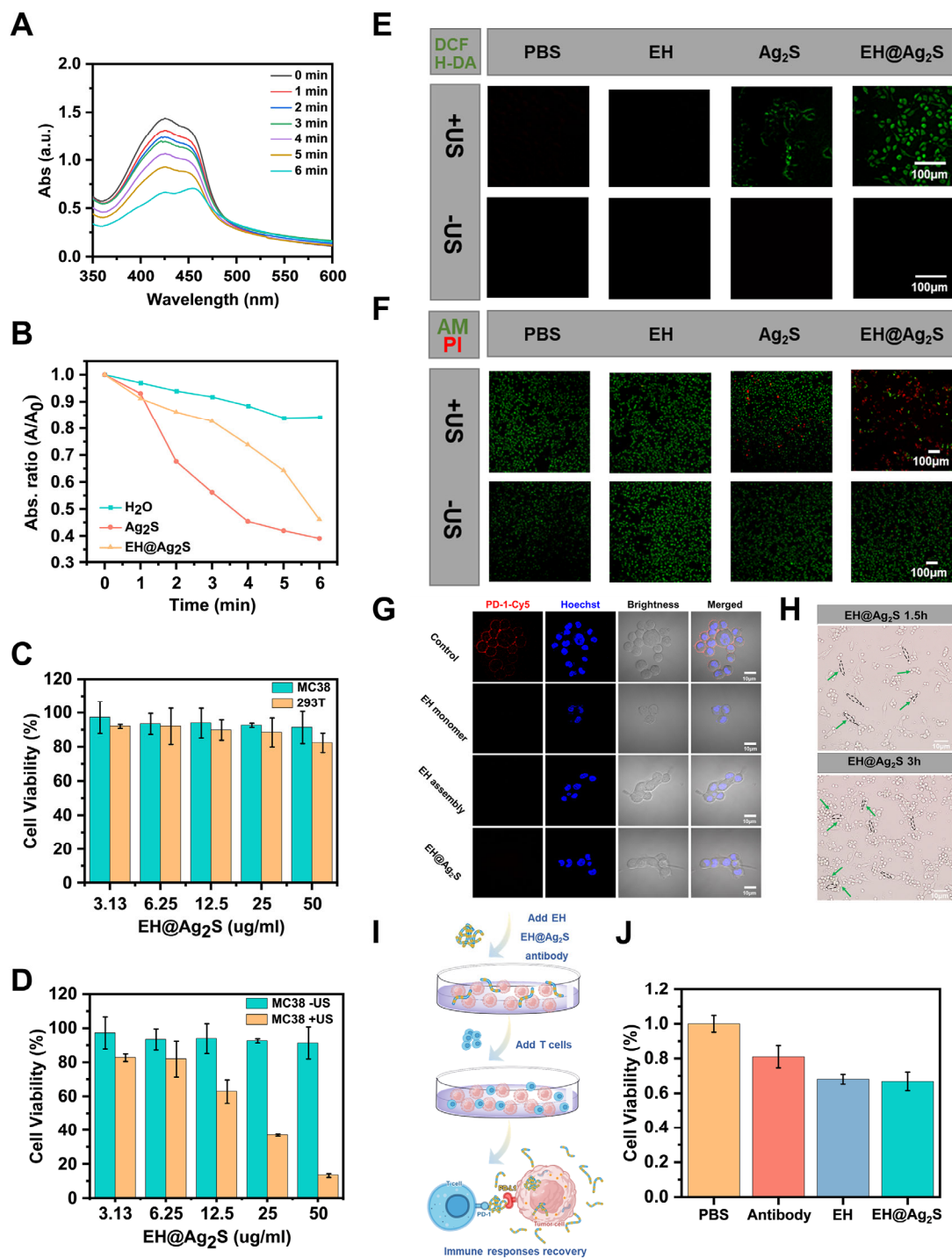


Fig. 3 *In vitro* SDT and immune checkpoint blockade therapeutic efficacy of EH@Ag₂S. **(A)** UV-vis absorption spectra of 1,3-diphenylisobenzofuran (DPBF) in the presence of EH@Ag₂S under prolonged US irradiation. **(B)** Comparison of the relative absorbance of DCFH-DA at 424 nm by H₂O, Ag₂S and EH@Ag₂S under US irradiation. **(C)** Cell viabilities of MC38 and HEK-293T cells after treatment with EH@Ag₂S at varied concentrations for the further 24 h incubation. **(D)** Cell viabilities of MC38 cancer cells after treatment with EH@Ag₂S at varied concentrations with/without US irradiation. **(E)** and **(F)** Confocal images of DCFH-DA-stained and Calcein AM/PI-stained contained MC38 cells after different treatments. **(G)** Confocal images of the

competition binding between PD-1/EH monomer, PD-1/EH assembly, and PD-1/EH@Ag₂S, respectively. **(H)** Illustration of the immunotherapy effect through co-culture experiment. **(I)** Schematic of the co-culture experiment of cancer cells and T cells. **(J)** Cell viabilities of MC38 cells after treatment with PBS, PD-L1 antibody, EH, and EH@Ag₂S for 48 h co-culture with T cells. Data were shown as mean \pm SD (n = 3).

3.4 *In vivo* antitumor effects of combination therapy

To further observe the synergetic interaction of EH@Ag₂S-mediated immune checkpoint blockade therapy and sonodynamic therapy *in vivo*, MC38 tumor-bearing mice models were employed to verify *in vivo* antitumor efficiency after receiving different treatments. The schematic depicting the experimental procedures was shown in **Fig. 4A**. In detail, treatment was initiated when the tumor volume reached $\sim 50 \text{ mm}^3$, female C57BL/6N mice bearing MC38 subcutaneous xenograft tumors were randomly divided into six groups: (1) PBS, (2) US, (3) Ag₂S +US, (4) PD-L1 antibody (5) EH and (6) EH@Ag₂S+US. At 6 h and 9 h after *i.v.* injection, mice in groups 2, 3 and 6 were treated with US irradiation (1.0 W cm^{-2} , 1.0 MHz, 50% duty free) for 3 min. During the treatment process, mice body weight and tumor volume in different treatment groups were measured and recorded every other day. After treatment, tumor photos of different groups were shown in **Fig. 4B**. Additionally, mice were imaged at 0, 7 and 14 days to monitor treatment effect (**Fig. 4C**). The tumor in EH@Ag₂S +US group were obviously smaller than in other treatment groups, and the tumor growth was significantly inhibited. The EH@Ag₂S +US group showed the most significant anti-tumor treatment effect, and tumor growth inhibition (TGI) index reached 98.4% compared with the PBS group as the grave and higher than the other groups (**Fig. 4E**). Consistent with the tumor growth data, tumor weight measurements also confirmed the tumor eradication effect of EH@Ag₂S +US group in tumor-bearing mice models (**Fig. 4E**). In general, Hematoxylin and eosin (H&E) staining and Terminal dUTP Nick End Labeling (TUNEL) staining were used to evaluate the pathological changes of tumor tissue after different treatments (**Fig. 4G**). For H&E staining, EH@Ag₂S +US group exhibited much greater cell damage and resulted in the highest apoptosis degree. Consistent with H&E staining results, TUNEL immunofluorescent staining also

indicated the most severe tumor necrosis and damage caused by EH@Ag₂S +US group, as indicated by the broadest distribution of green fluorescence. To assess the immune response after different treatments, the levels of tumor-infiltrating CD8⁺ T cells was examined in the tumor tissue by immunohistochemical (IHC) staining. As shown in **Fig. 4G**, the EH@Ag₂S +US-treated group obviously increased the CD8⁺ T cells in tumor, compared with other treatment groups indicating that ICB and SDT could enhance the infiltration of CD8⁺ T cells. In addition, interleukin-2 (IL-2) was detected to further examine the activity of the tumor-associated immune microenvironment. Comparing with other treatments, the expressions of T cells cytokines IL-2 increased mostly in the EH@Ag₂S +US-treated group. In order to further verify the immunomodulatory effect in different groups, IFN- γ and CRT were also detected. It is well-known that the activated CD8⁺ T cells can secrete immune cytokines like interferon- γ (IFN- γ) to kill tumor cells. In addition, calreticulin (CRT) is an important biomarker of ICD. The IHC staining results showed that EH@Ag₂S +US-treated group led to an increase in INF- γ and CRT expression, suggesting that they had the potential to induce an immune response through EH@Ag₂S-mediated both the immune checkpoint blockade therapy and sonodynamic therapy. These results suggested that the synergistic therapy showed more effective cytotoxic T cell response.

3.5 *In vivo* biocompatibility assay of EH@Ag₂S

Safety is also a top priority for the use of nanomedicines *in vivo*. **Fig. 4F** showed that the mice body weight in all groups was essentially unchanged and showed some increase during the treatment period, indicating the high biocompatibility and almost no toxicity of this system. In addition, the main organs in PBS group and EH@Ag₂S +US group, including the lung, liver, spleen, kidney and heart, were subjected to H&E staining after treatment. No significant necrosis or obvious organ damage was detected, further demonstrating the high biocompatibility of this system (**Fig. S8**). Moreover, to evaluate the long-term toxicity during the treatment period, blood routine and blood biochemical analysis were performed on mice treated with PBS group and EH@Ag₂S +US group. Compared with the PBS group, the concentration of primary hepatic and

renal function markers in EH@Ag₂S +US group, were within the normal reference ranges (Fig. S9, Fig. S10). These *in vivo* animal experiment results indicated that co-assembled EH@Ag₂S system with good biocompatibility had good antitumor effect and could activate immunity after treatment.

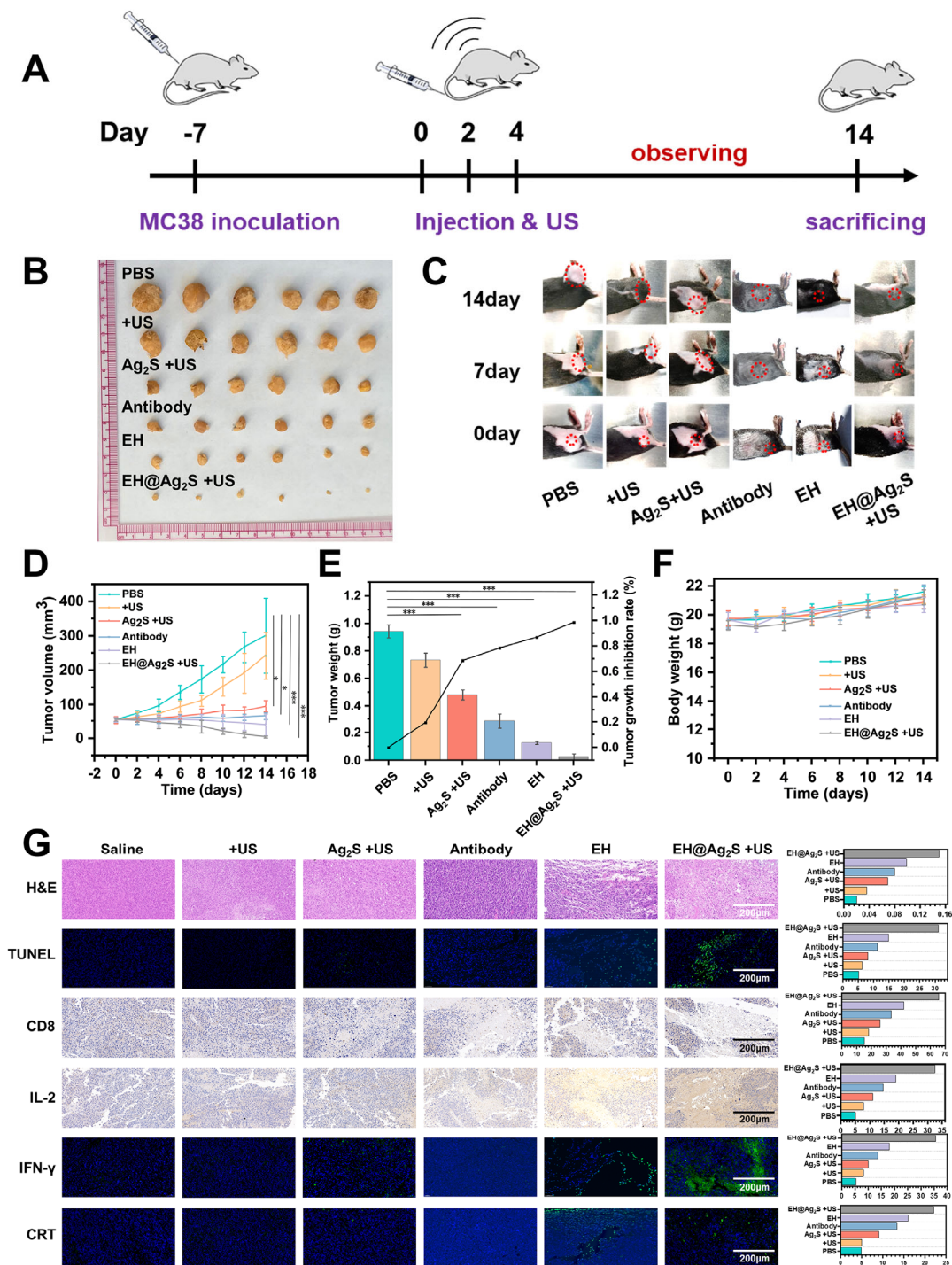


Fig. 4 *In vivo* therapy of EH@Ag₂S in MC38 tumor bearing mice. (A) Schematic illustration of the *in vivo* treatment schedule. (B) Images of excised tumors after different treatments. (C) Representative mice images in the different treatment groups

at 0, 7 and 14 days. The red circles represented the tumors. **(D)** Tumor growth curves of different groups of mice after different treatments (*, $P \leq 0.05$, **, $P \leq 0.01$, ***, $P \leq 0.001$). **(E)** Tumor-weight curves of mice and tumor growth inhibition (TGI) index after different treatments (*, $P \leq 0.05$, **, $P \leq 0.01$, ***, $P \leq 0.001$). **(F)** Body-weight curves of mice after different treatments. **(G)** H&E and TUNEL staining, as well as CD8, IL-2, IFN- γ and CRT immunohistochemical (IHC) staining analysis of tumor tissue after different treatments. Data were shown as mean \pm SD (n = 6).

3.6 Tumor genetic profile after tumor therapy

To deeply understand the antitumor mechanism of EH@Ag₂S under US irradiation and immunotherapy at the biomolecular level, RNA-sequencing (RNA-seq) technique analysis of tumor tissues after treatment was performed. Tumors in the PBS group, EH@Ag₂S and EH@Ag₂S +US were served as control. Key genes related to the PD-1/PD-L1 pathway were analyzed. For the EH@Ag₂S +US group, it down-regulated the PDCD1 gene, as well as other immune-related genes such as IDO1 and TP53, etc. (**Fig. 5C**). But for the EH@Ag₂S group, these results were not very obvious, we inferred that Ag₂S could generate ROS under US irradiation, thereby regulating the immune microenvironment, resulting in changes in the release of immune-related factors to exert anti-tumor effects. Genes involved in oxidative stress (**Fig. 5A**), such as SESN2, SLC7A11, and PRDX1, were significantly up-regulated by synergistic SDT and immune checkpoint blockade treatment. For tumor suppression and immune response processes, we mainly focused on genes related to tumor necrosis and apoptosis. The genes associated with tumor necrosis and apoptosis were up-regulated in EH@Ag₂S +US groups, such as TNFSF4, TNFSF10 and PSMB2, etc. (**Fig. 5B**). Then, to understand the molecular pathways affected by EH@Ag₂S +US group, Gene Ontology (GO) analysis and Kyoto Encyclopedia of Genes and Genomes (KEGG) were performed to identify molecular pathways and describe biological processes in transcriptional analysis data. As shown in **Fig. 5D** and **Fig. 5E**, we can clearly observe that the altered pathways are related with TNF signaling pathway, p53 signaling pathway and chemical carcinogenesis-reactive oxygen species in EH@Ag₂S +US group. These are signals for tumor apoptosis. These results all indicated the potential of the EH@Ag₂S +US group in terms of immune activation and anti-tumor.

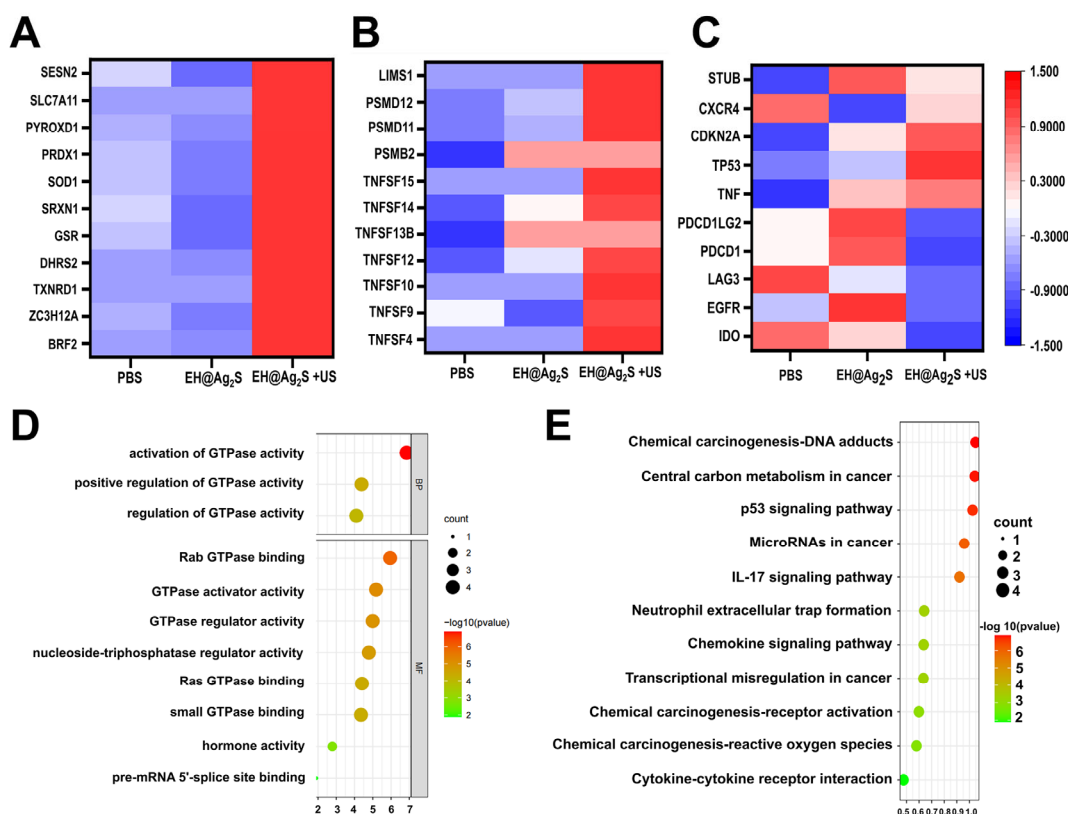


Fig. 5 Mechanism of EH@Ag₂S +US for combination therapy. **(A)**, **(B)** and **(C)** Heatmap of major genetic changes related to oxidative stress, tumor necrosis and apoptosis factor and immune response. **(D)** GO analysis of significantly altered genes. **(E)** KEGG analysis of significantly altered genes.

4. Conclusions

In summary, through rational design, we developed a peptide EH with both target recognition and self-assembly properties, and its affinity for PD-L1 is higher than its intrinsic receptor PD-1. EH can self-assembly into nanofibers, which enhanced the targeting and encapsulation on the PD-L1 flat surface. The formation of supramolecular assemblies ensures the stability of EH in the circulatory system. EH can exhibit different surface charges under different pH conditions of tumor microenvironment and tumor cells, ensuring the efficient co-assembly and spatiotemporal release of the sonosensitizer Ag₂S. The sonosensitizer Ag₂S can also generate a large amount of ROS under US irradiation. *In vitro* and animal experiments, the developed carrier-free co-assembled system EH@Ag₂S has showed satisfactory targeting, blocking ability and the ability to locally generate a large amount of ROS in tumor cells. These results all

demonstrated that the nano-sonosensitizer-enhanced SDT and PD-L1 checkpoint blockade had inhibitory activity against tumor development. This immune checkpoint blockade therapy combined with sonodynamic therapy model provides more possible avenues for future clinical cancer treatment.

Acknowledgments

The authors are grateful for financial support from National Natural Science Foundation of China (No. 22074006), Beijing Natural Science Foundation (No. 2222029) and Beijing Institute of Technology Research Fund Program for Young Scholars. We thank Analysis and Testing Center in Beijing Institute of Technology on the experimental data acquisition.

References

- [1] X. Wei, Z.Y. Feng, J.B. Huang, X. Xiang, F.X. Du, C. He, M. Zhou, L. Ma, C. Cheng, L. Qiu, homology and immune checkpoint dual-targeted sonocatalytic nanoagents for enhancing sonodynamic tumor therapy, *Acs Appl. Mater. Inter.* 13(28) (2021) 32810-32822.
- [2] M.M. Zhan, X.Q. Hu, X.X. Liu, B.F. Ruan, J. Xu, C.Z. Liao, From monoclonal antibodies to small molecules: the development of inhibitors targeting the PD-1/PD-L1 pathway, *Drug Discov. Today* 21(6) (2016) 1027-1036.
- [3] W.P. Zou, J.D. Wolchok, L.P. Chen, PD-L1 (B7-H1) and PD-1 pathway blockade for cancer therapy: mechanisms, response biomarkers, and combinations, *Sci. Transl. Med.* 8(328) (2016) 328rv4.
- [4] M.F. Sanmamed, L.P. Chen, A paradigm shift in cancer immunotherapy: from enhancement to normalization, *Cell* 175(2) (2018) 313-326.
- [5] A.V. Balar, J.S. Weber, PD-1 and PD-L1 antibodies in cancer: current status and future directions, *cancer immunol. Immunother.* 66(5) (2017) 551-564.
- [6] S. Li, W. Zhang, H. Xue, R. Xing, X. Yan, Tumor microenvironment-oriented adaptive nanodrugs based on peptide self-assembly, *Chem. Sci.* 11(33) (2020) 8644-8656.
- [7] M. Wang, L. Li, L. Zhang, J. Zhao, Z. Jiang, W. Wang, Peptide-derived biosensors and their applications in tumor immunology-related detection, *Anal. Chem.* 94(1) (2022) 431-441.
- [8] G.B. Qi, Y.J. Gao, L. Wang, H. Wang, Self-assembled peptide-based nanomaterials for biomedical imaging and therapy, *Adv. Mater.* 30(22) (2018) e1703444.
- [9] J.F. Li, Z.J. Chen, M.C. Zhou, J.B. Jing, W. Li, Y. Wang, L.X. Wu, L.Y. Wang, Y.Q. Wang, M. Lee, Polyoxometalate-driven self-assembly of short peptides into multivalent nanofibers with enhanced antibacterial activity, *Angew. Chem. Int. Edit.* 55(7) (2016) 2592-2595.
- [10] X.X. Han, K.M. Cheng, Y. Xu, Y.Z. Wang, H. Mm, Y.L. Zhang, X. Zhao, R.F. Zhao,

- G.J. Anderson, L. Ren, G.J. Nie, Y.Y. Li, Modularly designed peptide nanoprodug augments antitumor immunity of PD-L1 checkpoint blockade by targeting indoleamine 2,3-dioxygenase, *J. Am. Chem. Soc.* 142(5) (2020) 2490-2496.
- [11] S.S. Pillavi, H. Yukawa, D. Onoshima, V. Biju, Y. Baba, Forster resonance energy transfer mediated photoluminescence quenching in stoichiometrically assembled CdSe/ZnS quantum dot-peptide labeled black hole quencher conjugates for matrix metalloproteinase-2 sensing, *Anal. Sci.* 33(2) (2017) 137-142.
- [12] Z.Z. Yang, J.Q. Li, Z.Z. Wang, D.W. Dong, X.R. Qi, Tumor-targeting dual peptides-modified cationic liposomes for delivery of siRNA and docetaxel to gliomas, *Biomaterials* 35(19) (2014) 5226-5239.
- [13] K. Cheng, Y. Ding, Y. Zhao, S. Ye, X. Zhao, Y. Zhang, T. Ji, H. Wu, B. Wang, G.J. Anderson, L. Ren, G. Nie, Sequentially responsive therapeutic peptide assembling nanoparticles for dual-targeted cancer immunotherapy, *Nano Lett.* 18(5) (2018) 3250-3258.
- [14] X. Cun, J. Chen, M. Li, X. He, X. Tang, R. Guo, M. Deng, M. Li, Z. Zhang, Q. He, Tumor-associated fibroblast-targeted regulation and deep tumor delivery of chemotherapeutic drugs with a multifunctional size-switchable nanoparticle, *Acs Appl. Mater. Inter.* 11(43) (2019) 39545-39559.
- [15] R.J. Dong, Y.F. Zhou, X.H. Huang, X.Y. Zhu, Y.F. Lu, J. Shen, Functional supramolecular polymers for biomedical applications, *Adv. Mater.* 27(3) (2015) 498-526.
- [16] H. Cheng, Y.J. Cheng, S. Bhasin, J.Y. Zhu, X.D. Xu, R.X. Zhuo, X.Z. Zhang, Complementary hydrogen bonding interaction triggered co-assembly of an amphiphilic peptide and an anti-tumor drug, *Chem. Commun.* 51(32) (2015) 6936-6939.
- [17] R.F. Zou, Q. Wang, J.C. Wu, J.X. Wu, C. Schmuck, H. Tian, Peptide self-assembly triggered by metal ions, *Chem. Soc. Rev.* 44(15) (2015) 5200-5219.
- [18] L. Xu, Q. Shen, L.Z. Huang, X.D. Xu, H.Y. He, Charge-mediated co-assembly of amphiphilic peptide and antibiotics Into supramolecular hydrogel with antibacterial activity, *Front. Bioeng. Biotech.* 8 (2020) 629452.
- [19] M.W. Cao, S. Lu, N.N. Wang, H. Xu, H. Cox, R.H. Li, T. Waigh, Y.C. Han, Y.L. Wang, J.R. Lu, Enzyme-triggered morphological transition of peptide nanostructures for tumor-targeted drug delivery and enhanced cancer therapy, *Acs Appl. Mater. Inter.* 11(18) (2019) 16357-16366.
- [20] C.H. Ren, Y. Gao, Y. Guan, Z.Y. Wang, L.J. Yang, J. Gao, H.R. Fan, J.F. Liu, Carrier-free supramolecular hydrogel composed of dual drugs for conquering drug resistance, *Acs Appl. Mater. Inter.* 11(37) (2019) 33706-33715.
- [21] I.C. Li, A.N. Moore, J.D. Hartgerink, "Missing Tooth" multidomain peptide nanofibers for delivery of small molecule drugs, *Biomacromolecules* 17(6) (2016) 2087-2095.
- [22] Y.W. Han, Y.C. Zhang, S. Wu, M. Jalalah, S.A. Alsareii, Y.M. Yin, F.A. Harraz, G.X. Li, Co-assembly of peptides and carbon nanodots: sensitive analysis of transglutaminase 2, *Acs Appl. Mater. Inter.* 13(31) (2021) 36919-36925.
- [23] Z.Q. Su, H.Y. Shen, H.X. Wang, J.H. Wang, J.F. Li, G.U. Nienhaus, L. Shang, G. Wei, Motif-designed peptide nanofibers decorated with graphene quantum dots for

simultaneous targeting and imaging of tumor cells, *Adv. Funct. Mater.* 25(34) (2015) 5472-5478.

[24] Y. Mi, C.T. Hagan, B.G. Vincent, A.Z. Wang, Emerging nano-/microapproaches for cancer immunotherapy, *Adv. Sci.* 6(6) (2019) 1801847.

[25] L. Jerby-Arnon, P. Shah, M.S. Cuoco, C. Rodman, M.J. Su, J.C. Melms, R. Leeson, A. Kanodia, S. Mei, J.R. Lin, S. Wang, B. Rabasha, D. Liu, G. Zhang, C. Margolais, O. Ashenberg, P.A. Ott, E.I. Buchbinder, R. Haq, F.S. Hodi, G.M. Boland, R.J. Sullivan, D.T. Frederick, B. Miao, T. Moll, K.T. Flaherty, M. Herlyn, R.W. Jenkins, R. Thummalapalli, M.S. Kowalczyk, I. Canadas, B. Schilling, A.N.R. Cartwright, A.M. Luoma, S. Malu, P. Hwu, C. Bernatchez, M.A. Forget, D.A. Barbie, A.K. Shalek, I. Tirosh, P.K. Sorger, K. Wucherpennig, E.M. Van Allen, D. Schadendorf, B.E. Johnson, A. Rotem, O. Rozenblatt-Rosen, L.A. Garraway, C.H. Yoon, B. Izar, A. Regev, A cancer cell program promotes T cell exclusion and resistance to checkpoint blockade, *Cell* 175(4) (2018) 984-997.

[26] Z. Cao, D. Li, J. Wang, X. Yang, Reactive oxygen species-sensitive polymeric nanocarriers for synergistic cancer therapy, *Acta Biomater.* 130 (2021) 17-31.

[27] X.P. Duan, C. Chan, W.B. Lin, Nanoparticle-mediated immunogenic cell death enables and potentiates cancer immunotherapy, *Angew. Chem. Int. Edit.* 58(3) (2019) 670-680.

[28] K.M. Cheng, Y.P. Ding, Y. Zhao, S.F. Ye, X. Zhao, Y.L. Zhang, T.J. Ji, H.H. Wu, B. Wang, G.J. Anderson, L. Ren, G.J. Nie, Sequentially responsive therapeutic peptide assembling nanoparticles for dual-targeted cancer immunotherapy, *Nano. Lett.* 18(5) (2018) 3250-3258.

[29] S. Liang, X.R. Deng, G.Y. Xu, X. Xiao, M.F. Wang, X.S. Guo, P.A. Ma, Z.Y. Cheng, D. Zhang, J. Lin, A novel Pt-TiO₂ heterostructure with oxygen-deficient layer as bilaterally enhanced sonosensitizer for synergistic chemo-sonodynamic cancer therapy, *Adv. Funct. Mater.* 30(13) (2020) 1908598.

[30] S. Liang, X.R. Deng, P.A. Ma, Z.Y. Cheng, J. Lin, Recent advances in nanomaterial-assisted combinational sonodynamic cancer therapy, *Adv. Mater.* 32(47) (2020) e2003214.

[31] Y. Zheng, Y. Liu, F. Wei, H. Xiao, J. Mou, H. Wu, S. Yang, Functionalized g-C₃N₄ nanosheets for potential use in magnetic resonance imaging-guided sonodynamic and nitric oxide combination therapy, *Acta Biomater.* 121 (2021) 592-604.

[32] N. Auslander, G. Zhang, J.S. Lee, D.T. Frederick, B.C. Miao, T. Moll, T. Tian, Z. Wei, S. Madan, R.J. Sullivan, G. Boland, K. Flaherty, M. Herlyn, E. Ruppin, Robust prediction of response to immune checkpoint blockade therapy in metastatic melanoma, *Nat. Med.* 24(10) (2018) 1545-1549.

[33] P. Sharma, S. Hu-Lieskovan, J.A. Wargo, A. Ribas, Primary, adaptive, and acquired resistance to cancer immunotherapy, *Cell* 168(4) (2017) 707-723.

[34] Q.Y. Zhang, C.X. Bao, X.J. Cai, L.W. Jin, L.L. Sun, Y.H. Lang, L.B. Li, Sonodynamic therapy-assisted immunotherapy: a novel modality for cancer treatment, *Cancer Sci.* 109(5) (2018) 1330-1345.

[35] W.W. Yue, L. Chen, L.D. Yu, B.G. Zhou, H.H. Yin, W.W. Ren, C. Liu, L.H. Guo, Y.F. Zhang, L.P. Sun, K. Zhang, H.X. Xu, Y. Chen, Checkpoint blockade and

nanosensitizer-augmented noninvasive sonodynamic therapy combination reduces tumour growth and metastases in mice, *Nat. Commun.* 10(1) (2019) 2025.

[36] M.M. Guo, L.M. Zhang, Y.W. Tian, M.X. Wang, W.Z. Wang, Living-system-driven evolution of self-assembled-peptide probes: for boosting glioma theranostics, *Anal. Chem.* 93(22) (2021) 8035-8044.

[37] Y.W. Tian, L.M. Zhang, F.J. Liu, M.X. Wang, L.Y. Li, M.M. Guo, H.Y. Xu, Z.Y. Yu, W.Z. Wang, Multi-stage responsive peptide nanosensor: anchoring EMT and mitochondria with enhanced fluorescence and boosting tumor apoptosis, *Biosens. Bioelectron.* 184 (2021) 113235.

[38] P. Chen, Self-assembly of ionic-complementary peptides: a physicochemical viewpoint, *Colloid. Surface. a* 261(1-3) (2005) 3-24.

[39] R.V. Ulijn, A.M. Smith, Designing peptide based nanomaterials, *Chem. Soc. Rev.* 37(4) (2008) 664-675.

[40] Z. Chen, P.F. Zhao, Z.Y. Luo, M.B. Zheng, H. Tian, P. Gong, G.H. Gao, H. Pan, L.L. Liu, A.Q. Ma, H.D. Cui, Y.F. Ma, L.T. Cai, Cancer cell membrane-biomimetic nanoparticles for homologous-targeting dual-modal imaging and photothermal therapy, *Acs Nano* 10(11) (2016) 10049-10057.

[41] Y.N. Zhang, W. Poon, A.J. Tavares, I.D. McGilvray, W.C.W. Chan, Nanoparticle-liver Interactions: cellular uptake and hepatobiliary elimination, *J. Control. Rele.* 240 (2016) 332-348.

[42] Y.X. Tang, X.Y. Wang, J. Li, Y. Nie, G.J. Liao, Y. Yu, C. Li, Overcoming the reticuloendothelial system barrier to drug delivery with a "Don't-Eat-Us" strategy, *ACS Nano* 13(11) (2019) 13015-13026.

[43] R. Magnez, B. Thiroux, S. Taront, Z. Segaula, B. Quesnel, X. Thuru, PD-1/PD-L1 binding studies using microscale thermophoresis, *Sci. Rep.* 7(1) (2017) 17623-17630.

[44] X. Lin, X. Lu, G. Luo, H. Xiang, Progress in PD-1/PD-L1 pathway inhibitors: from biomacromolecules to small molecules, *Eur. J. Med. Chem.* 186 (2020) 111876.

[45] Y. Fan, X.D. Li, P.P. He, X.X. Hu, K. Zhang, J.Q. Fan, P.P. Yang, H.Y. Zheng, W. Tian, Z.M. Chen, L. Ji, H. Wang, L. Wang, A biomimetic peptide recognizes and traps bacteria *in vivo* as human defensin-6, *Sci. Adv.* 6(19) (2020) eaaz4767.

[46] L. Zhang, D. Jing, N. Jiang, T. Rojalin, C.M. Baehr, D.L. Zhang, W.W. Xiao, Y. Wu, Z.Q. Cong, J.J. Li, Y.P. Li, L. Wang, K.S. Lam, Transformable peptide nanoparticles arrest HER2 signalling and cause cancer cell death *in vivo*, *Nat. Nanotechnol.* 15(2) (2020) 145-153.

[47] K.N. Guye, H. Shen, M.Y. Yaman, G.Y. Liao, D. Baker, D.S. Ginger, Importance of substrate-particle repulsion for protein-templated assembly of metal nanoparticles, *Langmuir* 37(30) (2021) 9111-9119.

[48] C. Li, X.Q. Yang, J. An, K. Cheng, X.L. Hou, X.S. Zhang, Y.G. Hu, B. Liu, Y.D. Zhao, Red blood cell membrane-enveloped O₂ self-supplementing biomimetic nanoparticles for tumor imaging-guided enhanced sonodynamic therapy, *Theranostics* 10(2) (2020) 867-879.